Supporting Information:

Single-Molecule Ultrafast Fluorescence-Detected Pump–Probe Microscopy

Daniel Fersch[1], Pavel Malý[1,2], Jessica Rühe[3], Victor Lisinetskii[1], Matthias Hensen[1], Frank Würthner[3,4] and Tobias Brixner[1,4]*

[1]Universität Würzburg, Institut für Physikalische und Theoretische Chemie, Am Hubland, 97074 Würzburg, Germany

[2]Charles University, Faculty of Mathematics and Physics, Ke Karlovu 5, 121 16 Prague, Czech Republic

[3]Universität Würzburg, Institut für Organische Chemie, Am Hubland, 97074 Würzburg, Germany

[4]Universität Würzburg, Center for Nanosystems Chemistry (CNC), Theodor-Boveri-Weg, 97074 Würzburg, Germany

*brixner@uni-wuerzburg.de

S1. Spatial resolution

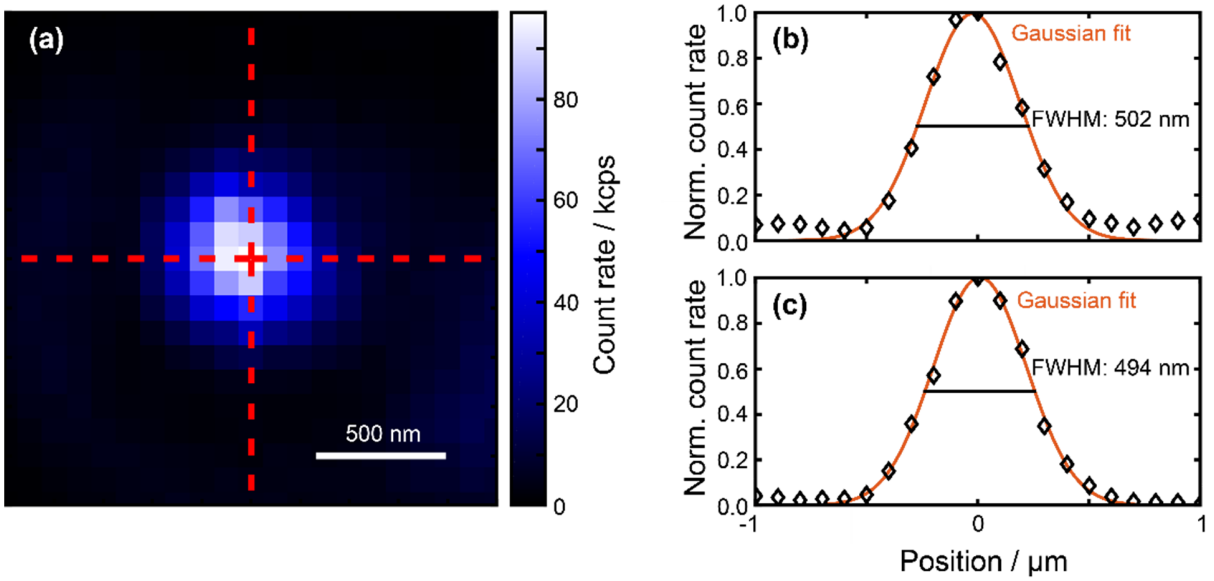

Figure S1. Demonstration of the spatial resolution of the microscope. (a) Scanned image of a fluorescent microsphere sampled with a step size of 100 nm. Cuts for cross sections are indicated with dashed red lines. (b, c) Cuts along horizontal (b) and vertical (c) direction (black diamonds) evaluated with a Gaussian fit (red solid) and the resulting FWHM as calculated from the standard deviation of the fit.

For demonstrating the spatial resolution of our microscope, we use spin-coated microspheres doped with fluorescent dyes (ThermoFisher, FluoSpheres™ F8807). They exhibit high photostability, and their sub-wavelength diameter of 200 nm enables us to approximate the microspheres as a point emitter in the analysis. The resolution of an ideal confocal microscope,

$$dx = 0.37\frac{\lambda}{\mathrm{NA}},$$

depends on the fluorescence wavelength λ and the numerical aperture (NA) of the detection objective.[1] This definition for resolution is somewhat arbitrary as it is derived from the distance at which two point emitters are separated at their full width at half maximum (FWHM), but is used frequently and we adopt it here as well. Considering the shortest fluorescence wavelength that we can measure with our setup (700 nm) and NA = 0.80, this yields $dx = 324$ nm as a theoretical expectation.

Experimentally, we cut the scanned microscope image in Figure S1a in vertical and horizontal directions to obtain cross sections. The central peak of the resulting one-dimensional Airy disk can then be approximated well with a Gaussian function. The standard deviation σ of the Gaussian is related to the FWHM definition of dx above by

$$dx = 2\sqrt{2ln2}\,\sigma,$$

which gives us $dx = 502$ and 494 nm for the horizontal and vertical cross sections, respectively.

The experimental resolution does not reach the theoretical, ideal limit, and we attribute this to several factors: First, no aberrations are considered in the imaging process. The theoretical value is further only valid for an infinitely small pinhole, which is not the case for our single-mode fiber with a mode field diameter of 3.6-5.3 µm. Last, the fluorescent bead emits at a broad range of wavelengths larger than 700 nm. All three factors are not considered in the calculation of the theoretical resolution, meaning that this calculation only yields a fundamental lower limit, and our measured values are already close to what can be reached with our setup.

S2. Pulse characterization at the sample position

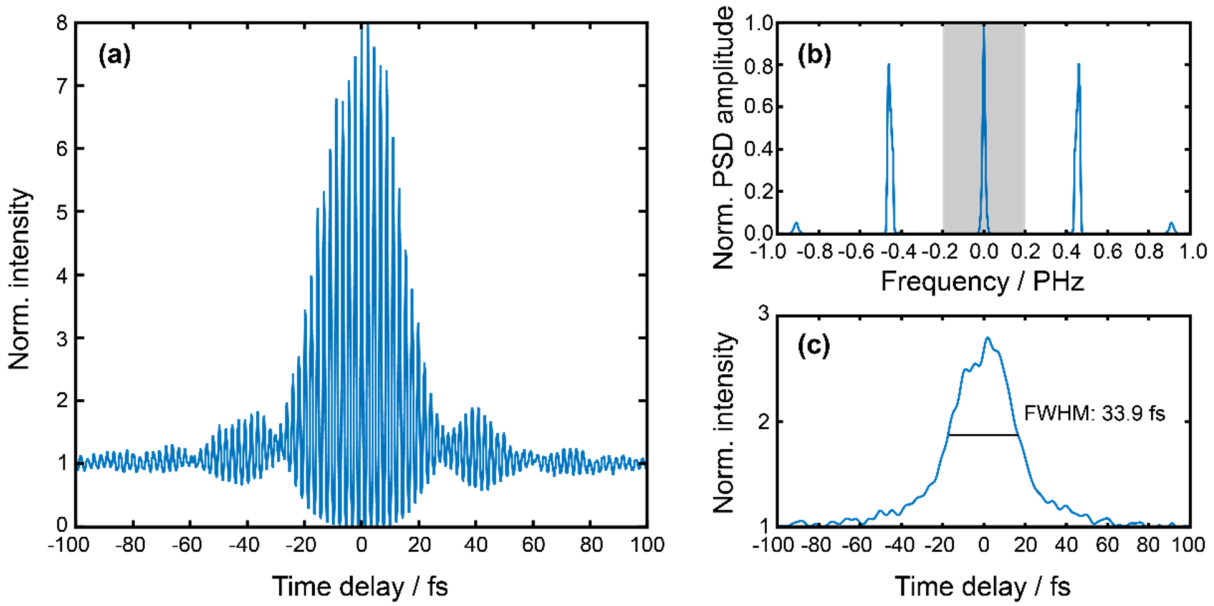

Figure S2. Temporal resolution of the F-PP microscopy setup. (a) Second-order nonlinear interferometric autocorrelation measured at the sample position using two-photon absorption in a photodiode. The signal was normalized to large time delays. (b) Power spectrum obtained after Fourier transformation of the interferometric autocorrelation. The shaded area indicates the area of the spectrum that was filtered. (c) Inverse Fourier transformation of the shaded grey area in (b), yielding an intensity autocorrelation. The FWHM is indicated by the black line.

We use two-photon absorption in a GaP photodiode (Roithner Lasertechnik, EPD-440-0/0.9) to characterize the pulses at the focus position of the microscope objective and record a second-order nonlinear interferometric autocorrelation of the pump pulse (Figure S2a). The pulse shaper was used to generate the required pulse pair including time delays. This signal can be decomposed into several frequency components with the power spectrum shown in Figure S2b. We use a rectangular frequency window filter (grey shaded) to keep only the zero-frequency component.[2] After inverse Fourier transformation, we recover an intensity autocorrelation (Figure S2c). The FWHM and assuming a Gaussian pulse shape yields a pulse duration of 24 fs. While the pulses shape is obviously not Gaussian, as can be seen from the "wings" in Figure S2a, we use the recovered value as a reasonable estimate only of the duration.

The measurement was repeated for both probe pulses and yielded similar results. This was expected because the only difference between pump and probe beam paths consisted in few mirrors and thin, group-velocity-dispersion-compensated beam splitters in the interferometer.

S3. Morphology of the ensemble sample

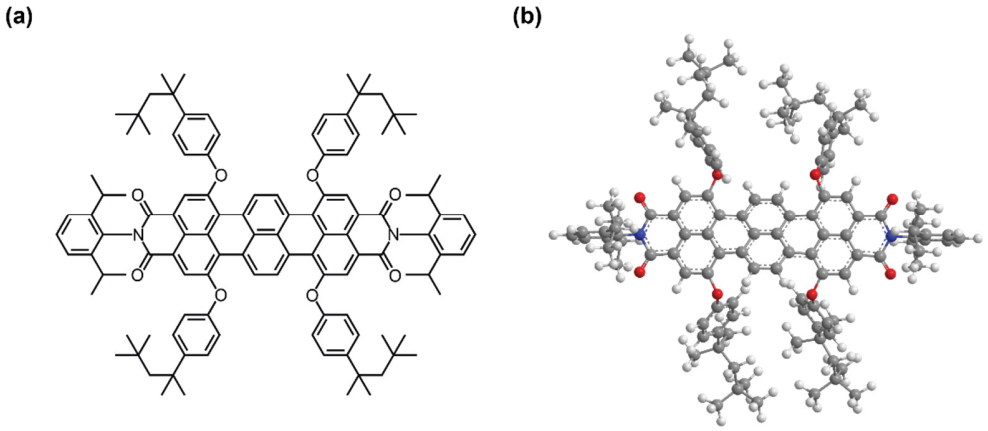

Figure S3. (a) Structural formula of TBI with all substituents explicitly drawn. (b) Three-dimensional geometry of TBI as obtained from a molecular mechanics simulation displayed as a ball-and-stick model, including the (1,1,3,3-tetramethylbutyl) groups not included in the quantum-chemical simulation.

We discuss the properties of the ensemble sample here because spin coating can lead to self-assembled and heavily disordered samples. One parameter often used to label samples of dye-doped polymer matrices is the mass fraction (or percentage by weight, wt%) of dye to polymer, with higher mass fractions favoring aggregation between dyes. We used the values in Table S1 to calculate the mass ratios in this work.

c_{TBI} / µmol l^{-1}	M_{TBI} / g mol^{-1}	$\rho_{C_6H_5Cl}$ / g ml^{-1}	w_{PMMA}	$V_{C_6H_5Cl}$ / µl	V_{total} / µl
2.196	1652.27	1.109	0.02	5	10

Table S1. Values used for calculating the masses of TBI and PMMA in the solution droplet used for spin coating, including the concentration of the TBI solution, TBI molar mass, density of chlorobenzene, solids content of PMMA, as well as the volumes of chlorobenzene and the full solution.

As illustrated in the main manuscript, 10 µl of a diluted solution consisting of TBI/PMMA in toluene/chlorobenzene was used for spin coating. The total mass of TBI in the solution can be obtained from the concentration, molar mass, and total volume by

$$m_{TBI} = c_{TBI} M_{TBI} V_{total},$$

yielding a total mass of 36.82 ng.

For the total mass of PMMA, the solids content (equivalent to the mass fraction of PMMA to chlorobenzene) was used as specified by the manufacturer, which can then be calculated by

$$m_{PMMA} = w_{PMMA}\, \rho_{C_6H_5Cl}\, V_{C_6H_5Cl},$$

yielding a total mass of 111 µg.

Comparing both masses yields a mass fraction of 0.03% for our ensemble sample. Previous work on the influence of the mass fraction on aggregation for similar rylene dyes has shown that aggregation effects on the absorption and emission spectra become relevant at mass fractions of 0.5% and higher.[3] Our dye-to-polymer ratio is over an order of magnitude lower, making dye aggregation in the matrix very unlikely.

Further, in the TBI molecules used in this work, both the imide positions as well as all four bay positions are substituted with bulky aryl moieties, with the full structure shown in Figure S3a. To illustrate the three-dimensional structure, the geometry of TBI as obtained from a molecular mechanics simulation (using the

MM2 force field method implemented in CambridgeSoft ChemBio3D) is shown in Figure S3b. The 4-(1,1,3,3-tetramethylbutyl)-phenoxy groups in the bay positions extend far from the core with many degrees of freedom, while the 2,6-diisopropylphenyl groups in the imide positions show perpendicular orientation to the terrylene backbone. It is known from literature that this sterical hindrance strongly discourages self-assembly into aggregates in solution, to the point where perylene dyes with identical substitution have been used as purely monomeric reference compounds.[4,5] It should be noted that the structure shown in Figure S3b is only one of many conformations due to the many degrees of freedom in the long alkyl chains and is used mainly for illustration purposes.

From these two points we exclude aggregation effects in our ensemble sample. Instead of a thin film with aggregated dyes, the ensemble sample consists of PMMA with many dyes dispersed into the polymer matrix. While these molecules are still well-separated on a nanoscopic scale and do not interact with each other, many of them are captured by the diffraction-limited focus of our microscope, thus providing intrinsic ensemble averaging. This explains the lack of spatial heterogeneity in the microscope image shown in Figure 2b. Additionally, this is why we can reproduce the measured linear spectrum of the spin-coated sample by multiplying the liquid-phase absorption spectrum and the laser spectrum, as demonstrated in Figure 2b. In the case of aggregation, the absorption spectrum of the resulting film should change, ultimately leading to a linear spectrum that could not be reproduced by this procedure.

S4. Estimation of the noise floor of F-PP spectra

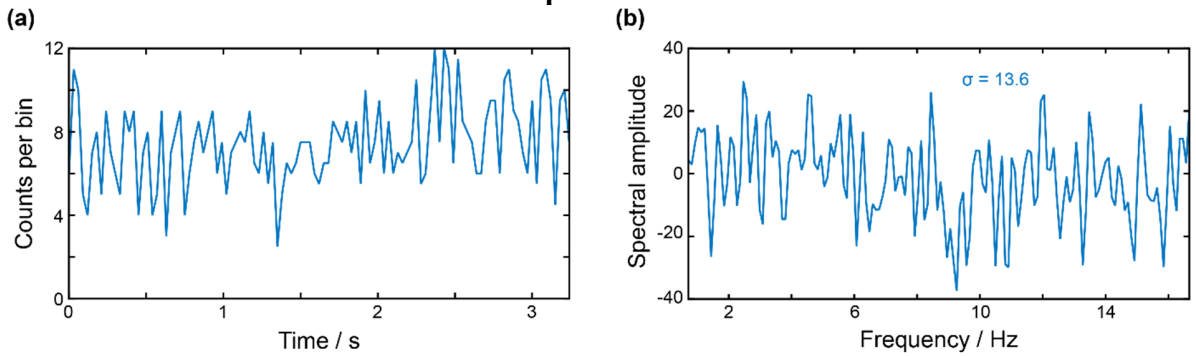

Figure S4. Estimation of the noise floor of F-PP spectra by analyzing the residual signal of a spin-coated sample after permanent photobleach. (a) Residual signal counts per binning interval (blue) after permanent photobleach of a single molecule recorded by continuously illuminating the same sample spot with the pump pulse. (b) Real part of the spectrum (blue) as obtained by Fourier transforming the trace in Figure S4a. The standard deviation of the spectrum in the shown region is given as a number.

To give a quantitative measure for the noise floor of the F-PP spectra shown in Fig. 3 and Fig. 5 we continuously illuminated a single molecule with the pump pulse until irreversible photobleach and recorded the remaining background signal (Figure S4a). The integration time of the photon counter (serving as a bin for each data point) and the length of this temporal trace were kept identical to the measured spectra in the main manuscript. We then zero-padded and Fourier transformed this temporal trace as we did for the linear and F-PP spectra (see Methods), obtaining a noise spectrum (Figure S4b). The standard deviation for this noise spectrum is 13.6.

To convert this value into the noise floor for each F-PP spectrum we first scaled it by a factor of $\sqrt{2}$, which results from error propagation as the F-PP spectrum is obtained from the difference of two interferograms. We then compensated for the 10-times averaging of temporal bins performed during acquisition of the F-PP spectra, which was performed to increase the signal-to-noise ratio, by further scaling the error value by $\frac{1}{\sqrt{10}}$. As the F-PP spectra illustrated in Figure 3b and Figure 5b were averaged over the waiting time, we compensated for the varying amount of waiting time steps with an additional factor of $\frac{1}{\sqrt{n_T}}$ ($n_T = \sqrt{27}$ and $n_T = \sqrt{14}$ for Figure 3b and Figure 5b, respectively). Finally, we multiplied the error value by the constant scaling factor that was applied to the F-PP spectra in the main text (see Methods), resulting in final values for the noise floor of 9.6×10^{-6} and 2.9×10^{-3} for the ensemble and single-molecule measurements in Figure 3b and 5b, respectively.

S5. Synthesis and characterization of TBI

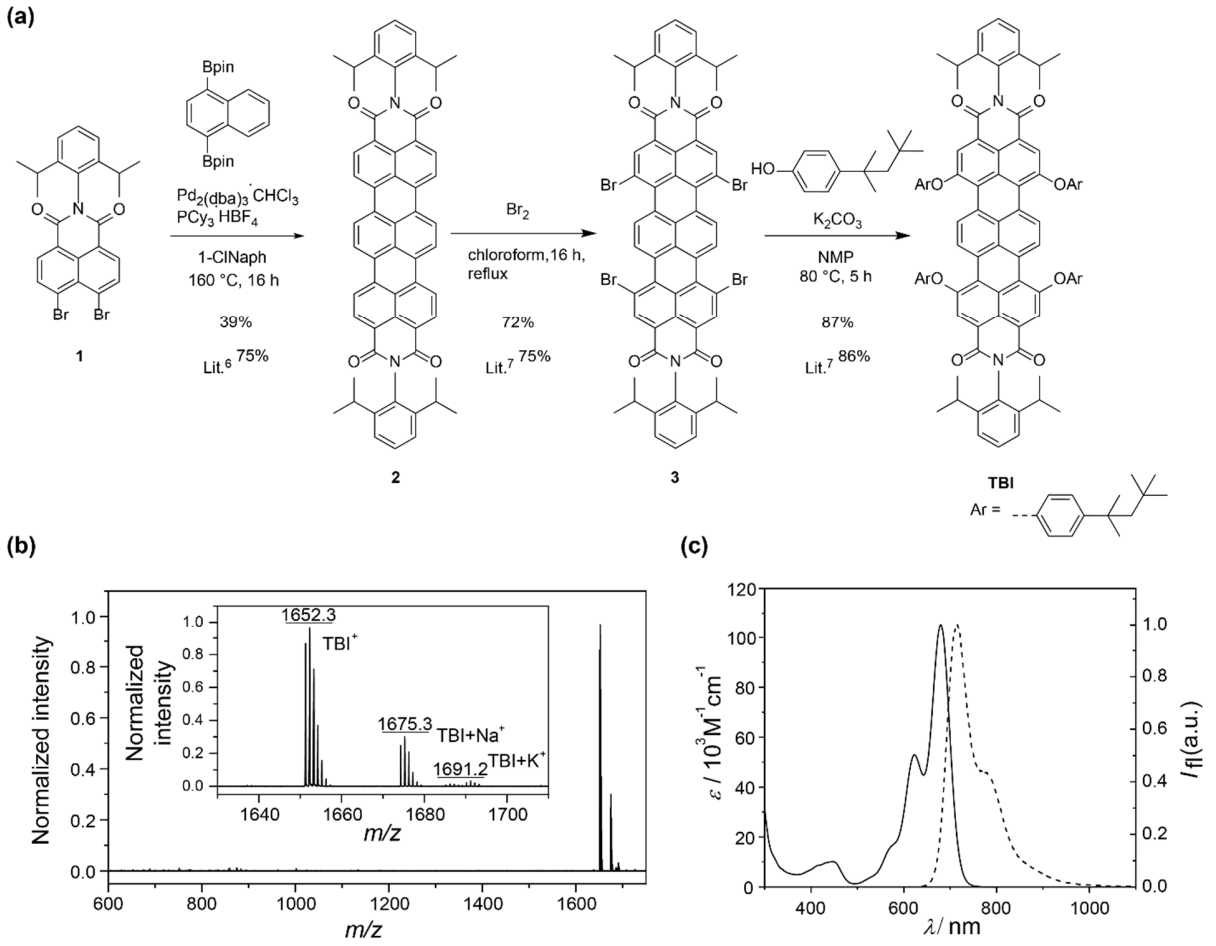

Figure S5. Synthesis and characterization of **TBI**. (a) Synthetic route towards **TBI** including the unsubstituted and brominated precursor. (b) Mass spectrum (MALDI-TOF, matrix: DCTB in chloroform, 1:1) of **TBI**. The inset shows a zoom-in to the signals corresponding to **TBI**. The mass spectrum has been normalized to the largest peak at 1652.3 m/z. (c) Steady-state UV/Vis absorption (solid) and fluorescence (dashed, λ_{ex} = 620 nm) spectra of **TBI** in chloroform at 293 K.

Terrylene bisimide **TBI** was synthesized according to literature by synthesis of the unsubstituted terrylene bisimide,[6] following bromination[7] and substitution[7] as shown in Figure S5a. The last purification step of **TBI** was precipitation from dichloromethane with *n*-hexane and filtration. After synthesis, the compound was characterized using MALDI-TOF mass spectrometry (Figure S5b), UV/Vis absorption spectroscopy (Figure S5c), steady-state fluorescence spectroscopy (Figure S5c), and ^{1}H-NMR spectroscopy. Technical details for these methods as well as experimental values from characterization are given in the following.

UV/Vis absorption spectroscopy: All spectroscopic measurements were carried out under ambient conditions using solvents of spectroscopic grade. The absorption spectra were recorded on a JASCO V-770 spectrometer equipped with a PAC-743R Peltier for temperature control.

UV/Vis ($CHCl_3$): λ_{max} (ε) = 679 (105300 $M^{-1}cm^{-1}$), 623 (52900 $M^{-1}cm^{-1}$); Lit[7]: λ_{max} (ε) = 679 (99 716 $M^{-1}cm^{-1}$), 624 (50 721 $M^{-1}cm^{-1}$).

Steady-state fluorescence spectroscopy: Fluorescence spectra were recorded on an Edinburgh Instruments FLS980 fluorescence spectrometer. The fluorescence quantum yield (Φ_{fl}) was determined by averaging the value for four different excitation wavelengths relative to Rhodamine 800 (Φ_{fl} =0.25 in ethanol)[8] as a standard under highly diluted conditions (OD ≤ 0.05).

Fluorescence (toluene): $\lambda_{em,\,max}$ = 707 nm (Φ_{fl} =0.60, Lit.[7] 0.53±0.1).

NMR spectroscopy: ^{1}H-NMR spectra were recorded on a Bruker Avance III HD 400 spectrometer at 298 K. Chemical shift data are reported in parts per million (ppm, δ scale) downfield from tetramethylsilane and referenced internally to the residual proton (for proton NMR) in the solvent ($CDCl_3$: δ = 7.26).

^{1}H NMR (400 MHz, $CDCl_3$): 9.51 (s, 4H), 8.29 (s, 4H), 7.43 (m, 10H), 7.29 (d, *J*=7.8 Hz, 4H), 7.11 (d, J=8.8Hz, 8H), 2.71 (h, 4H), 1.73 (s, 8H), 1.38 (s, 24H), 1.11 (d, *J*=6.8Hz, 24H), 0.73 (s, 36H) ppm.

Mass spectrometry: Mass spectra were recorded on a Bruker Daltonics ultrafleXtreme mass spectrometer using DCTB as a matrix for MALDI-TOF.

MS (MALDI-TOF, positive): $[M]^+$ calculated for $C_{114}H_{126}N_2O_8^+$, 1650.951, found: 1651.265.

S6. F-PP measurement without sample

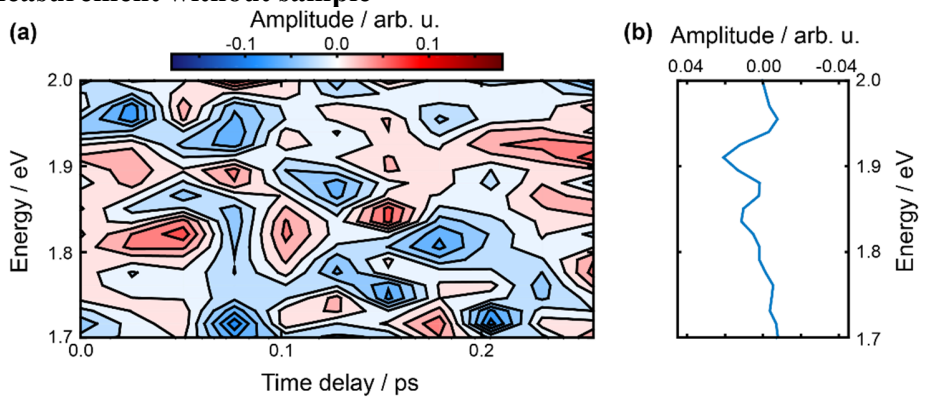

Figure S6. F-PP measurement without sample. (a) F-PP spectrum of the laser measured by removing the long-pass filters and detecting the transmitted pulse train. Delays were sampled from 0 to 0.25 ps in 25 fs steps. (b) F-PP spectrum averaged over all T steps to demonstrate the lack of signal even after averaging when no sample is in the microscope.

As nonlinear signals from single molecules will in general be extremely low, it is possible that artifacts from the measurement process might significantly contribute to or even dominate the measured F-PP spectrum. One such artifact is nonlinear behavior of the detector.

To exclude this kind of nonlinearity, we performed a control measurement without a sample in the fluorescence microscope, where we removed the long-pass filters in front of the photon counter to directly detect the transmitted pulse train. The resulting F-PP spectrum is seen in Figure S6a.

This spectrum is unstructured and consists of pure noise, where no significant signal contributions or temporal evolution as expected from a pump–probe measurement are observed. As the time-averaged spectra are also discussed in the main manuscript, we performed the same averaging for this spectrum, with the result shown in Figure S6b. Again, no structured spectrum can be seen. It should be noted that the amplitude of the signal cannot be compared to the spectra in the main manuscript as there is an additional pointing instability in the pump beam originating from the vibrational motor used to remove the coherence between the pump pulse and the probe pulse pair. This instability is not relevant in the focus of the microscope as a single molecule is much smaller than the diffraction-limited focus, and the molecular fluorescence does not exhibit this pointing instability. Still, we can conclude from this measurement that even in the weak nonlinear spectra and transients we observe for single molecules, they are not distorted or even dominated by artifacts originating from nonlinear detection.

S7. Explanation of red shift seen in the linear spectra of single molecules

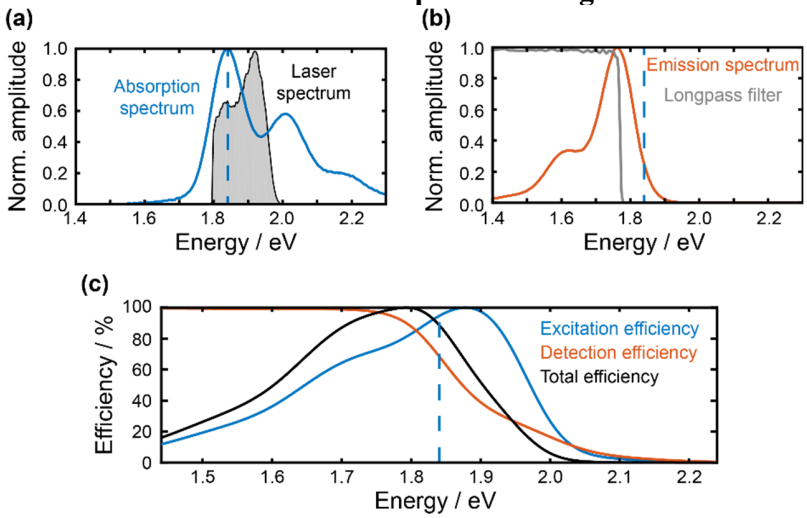

Figure S7. Analysis of spectral measurement efficiency. (a) Laser spectrum (grey) and unshifted absorption spectrum (blue). The absorption peak is marked with a vertical dashed line. (b) Long-pass filter transmission (grey) and unshifted emission spectrum (orange). The blue dashed line is the same as in (a). (c) Efficiency curves for excitation (blue), detection (orange), and their product (black). All curves are normalized to their individual maximum. The dashed blue line provides the energy reference indicated in (a) and (b).

In the main manuscript, the single-molecule linear spectra are systematically red-shifted in comparison to the ensemble reference. We attribute this shift to a selection bias in our single-molecule samples: Only the brightest molecules were measured, whereas no such selection was performed for the ensemble sample.

In general, the total measured brightness of a molecule is determined by the efficiencies of excitation and detection and the fluorescence quantum yield. As the local environment of a single molecule can affect the position of its absorption and emission spectrum, this can lead to a variation in the excitation and detection efficiency for each molecule, resulting in a variation in recorded brightness. This is not the case for any ensemble measurement, as this variation is intrinsically averaged out over many molecules.

In our case, the excitation efficiency is determined by the overlap of the laser spectrum and the absorption spectrum (Figure S7a), while the detection efficiency is determined by the overlap of the emission spectrum and the transmission window of the long-pass filter used for isolating the fluorescence (Figure S7b) as well as the photon counter detection efficiency (which we assume to be constant over the relevant range in the following). We show the excitation/detection efficiency along with their product as a function of the energetic position of the absorption/emission spectrum while assuming a constant Stokes shift and fluorescence quantum yield (Figure S7c). In addition, the energetic position of the ensemble absorption spectrum is shown as a reference.

The maximum of the total efficiency curve (Figure S7c, black) is observed at a lower energy than the unshifted ensemble reference (blue dashed). From this we conclude that, on average, single molecules with a red-shifted absorption spectrum will display more photon counts in our microscope images. As we selected for the brightest single molecules in our measurements, this selection bias will then lead to the observed red-shift in the histogram in Figure 4d when comparing the first moments of the linear spectra of single-molecules in contrast to the ensemble reference.

S8. Mean linear and F-PP spectra used for statistical analysis

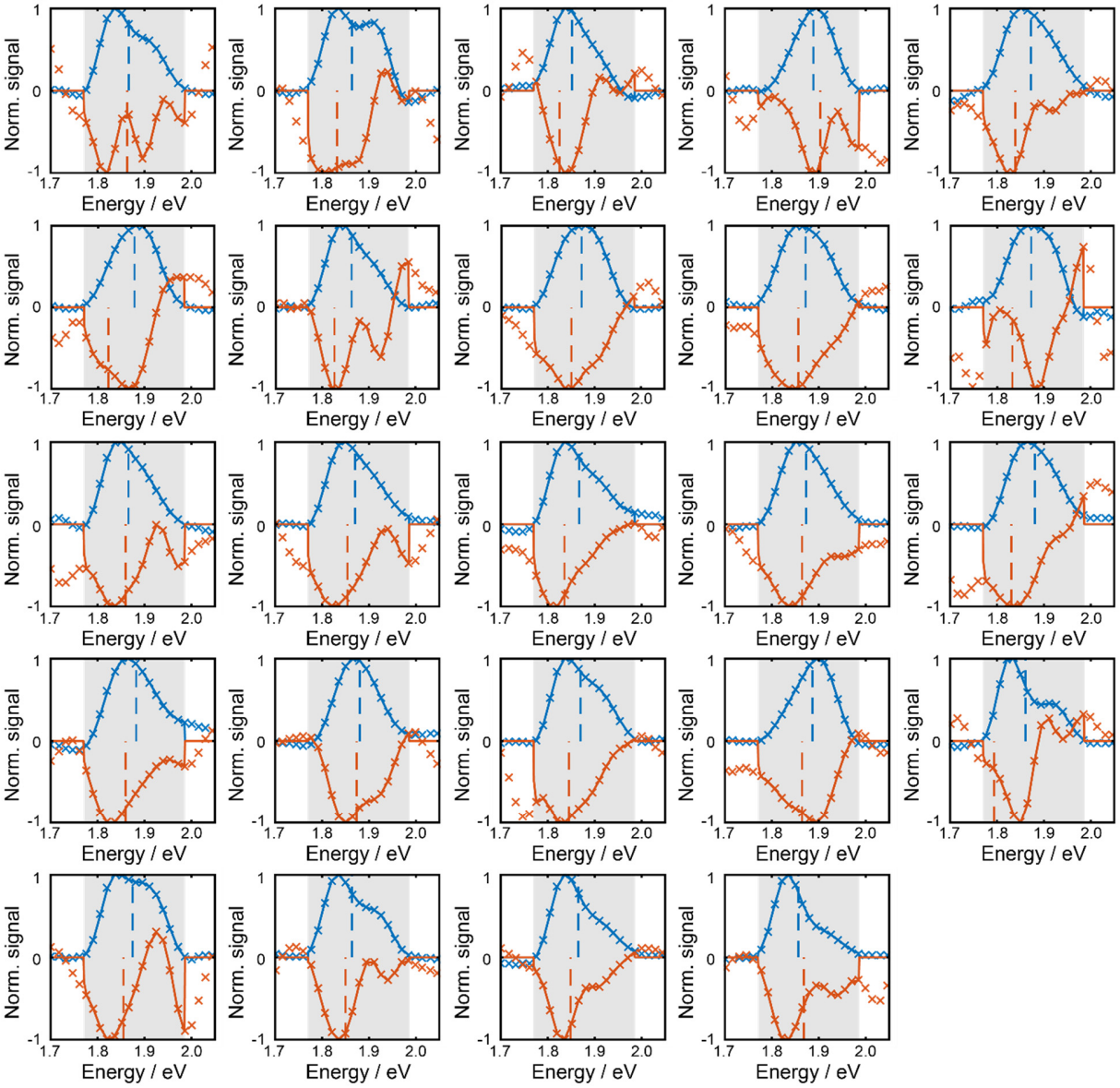

Figure S8. Mean F-PP (red) and linear (blue) spectra of 24 single molecules. The individual data points for each spectrum are given as colored scatter points. The spectra that were used for statistical analysis, with values outside of the signal window (shaded in grey) set to zero, are given as solid lines, with the resulting first moments shown as dashed lines. Signal amplitudes have been normalized for visual purposes.

In the main manuscript, we correlate the first moments of F-PP and linear spectra for 24 single molecules. To calculate the first moments, we first defined a signal window (which is identical to the signal window in the main manuscript), which is shown as a grey box in Figure S8. We then discarded all waiting time steps where the F-PP spectrum showed an average signal larger than zero inside of this signal window. This evaluation step is justified as we know from the reference measurement (Fig. 3a) that we cannot expect peaks with positive sign, meaning that these waiting time steps are too noisy to be evaluated.

The F-PP spectra along with the linear spectra of the same molecules after averaging over the waiting time T are shown in Figure S8 as individual data points. To further reduce the influence of the noisy baseline on the moment calculation, we additionally set all values outside of the signal window to 0, with the resulting spectra shown as solid lines. The corresponding first moments are displayed as dashed lines.

S9. Systematic red shift in the first moments of linear and F-PP spectra

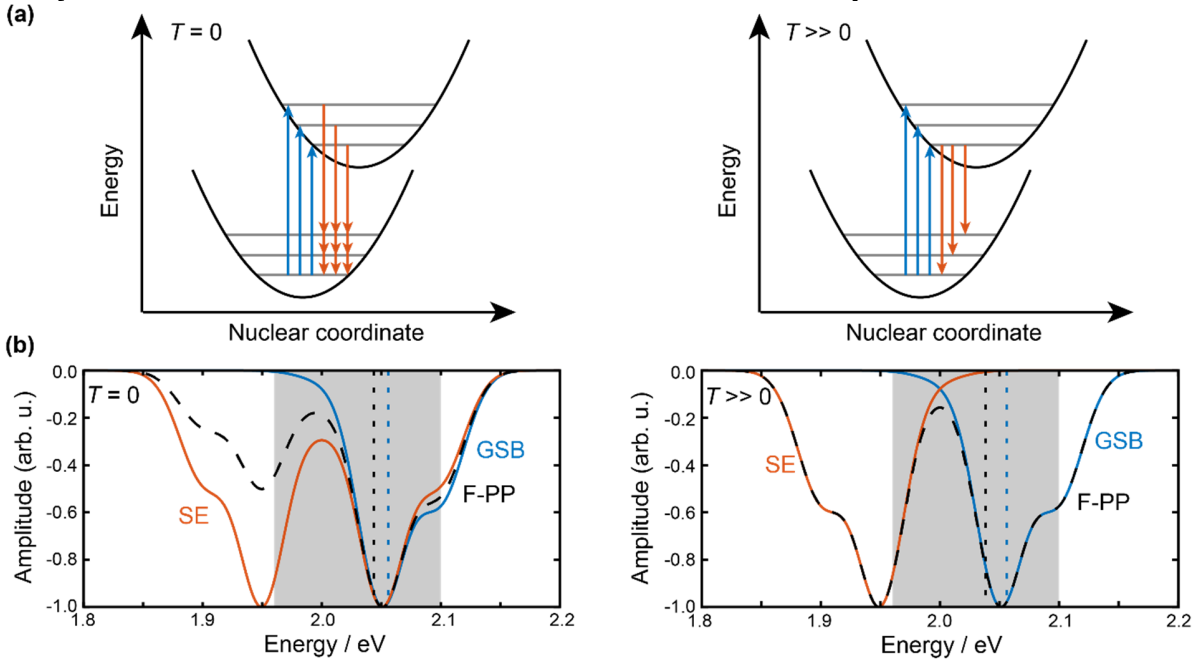

Figure S9. Explanation of systematic red shift using a model of two displaced harmonic oscillators. (a) Two harmonic oscillators displaced along a general nuclear coordinate, representing a ground (bottom black parabola) and excited electronic state (upper black parabola) with vibrational sublevels. Exemplary transitions from the ground to the excited state (blue) and vice versa (red) are given before (left) and after (right) vibrational relaxation. (b) Sketch of F-PP spectra (dashed black) resulting from ground-state bleach (GSB, blue) and stimulated emission (SE, red) contributions before (left) and after (right) vibrational relaxation. The first moment of the GSB contribution (dotted blue) and the F-PP spectrum (dotted black) within a limited signal window (shaded grey) are given in addition, demonstrating the systematic red shift. Note that the spectra are merely sketched for demonstration purposes and do not result from any simulated or measured data.

In the F-PP spectrum discussed in the main manuscript, both ground-state bleach and stimulated emission contributed to the observed signal. We then correlated the first moments of the linear and nonlinear spectrum against each other, observing both a systematic red shift as well as significant linear correlation between both moments. We explained this observation by modeling the dye system as two harmonic oscillators.

This is illustrated in detail in Figure S9a, where the electronic ground and first excited state are sketched as two harmonic oscillators with three vibrational sublevels each. The electronic transitions for absorption and spontaneous emission are given as blue and red arrows, respectively. In addition, both harmonic oscillators are displaced from each other along a generalized nuclear coordinate because the equilibrium geometries for the ground and excited state are not identical. The resulting spectra for absorption and emission are then given not only by the individual transition frequencies but are additionally weighted by the overlap between the wavefunctions of the associated vibrational sublevels, commonly referred to as Franck–Condon factors, which are heavily dependent on this nuclear displacement.

Relating this to the spectra that are discussed in the main manuscript, the ground-state bleach contribution is generally equivalent to the linear spectrum, as it is caused by transitions from the ground to the excited state. The case for the stimulated emission contribution is a bit more complex. After initial excitation, stimulated emission is generally possible for all vibronic transitions (Figure S9a, left), provided they are covered by the laser spectrum. As the system vibrationally relaxes, the number of transitions is reduced, and is finally equivalent to the number of transitions involved in spontaneous emission (Figure S9a, right). This is intuitive as for both stimulated emission after vibrational relaxation and spontaneous emission, the transition can only occur from the lowest vibrational state of the excited electronic state, provided Kasha's

rule is fulfilled in the molecular system. Figure S9b illustrates a sketch of ground-state bleach, stimulated emission, as well as a sum of both (which is equivalent to the F-PP spectrum) for $T = 0$ (left) and $T \gg 0$ (right). To relate these sketched spectra to our data, we calculated the first moment of the F-PP spectrum and the ground-state bleach contribution (which is equivalent to the linear spectrum) inside of a limited probe window before and after vibrational relaxation. When comparing these moments, the first moment of the F-PP spectrum is shifted to lower energies due to the additional stimulated emission contribution for both $T = 0$ and $T \gg 0$. This model explains why we see a systematic red shift when comparing the first moments of linear and F-PP spectra (Figure 5e).

References

(1) Kubitscheck, U. *Fluorescence Microscopy: From Principles to Biological Applications*; Wiley-VCH Verlag GmbH & Co. KGaA: Weinheim, Germany, 2013.

(2) Wollenhaupt, M.; Assion, A.; Baumert, T. Femtosecond Laser Pulses: Linear Properties, Manipulation, Generation and Measurement. In *Springer Handbook of Lasers and Optics*; Träger, F., Ed.; Springer Science+Business Media: New York, 2007; pp 937–983.

(3) Ramírez, M. G.; Morales-Vidal, M.; Navarro-Fuster, V.; Boj, P. G.; Quintana, J. A.; Villalvilla, J. M.; Retolaza, A.; Merino, S.; Díaz-García, M. A. Improved Performance of Perylenediimide-Based Lasers. *J Mater Chem C* **2013**, *1*, 1182–1191.

(4) Nowak-Król, A.; Würthner, F. Progress in the Synthesis of Perylene Bisimide Dyes. *Org. Chem. Front.* **2019**, *6*, 1272–1318.

(5) Chen, Z.; Stepanenko, V.; Dehm, V.; Prins, P.; Siebbeles, L. D. A.; Seibt, J.; Marquetand, P.; Engel, V.; Würthner, F. Photoluminescence and Conductivity of Self-Assembled π–π Stacks of Perylene Bisimide Dyes. *Chem. - Eur. J.* **2007**, *13*, 436–449.

(6) Shoyama, K.; Mahl, M.; Seifert, S.; Würthner, F. A General Synthetic Route to Polycyclic Aromatic Dicarboximides by Palladium-Catalyzed Annulation Reaction. *J. Org. Chem.* **2018**, *83*, 5339–5346.

(7) Nolde, F.; Qu, J.; Kohl, C.; Pschirer, N. G.; Reuther, E.; Müllen, K. Synthesis and Modification of Terrylenediimides as High-Performance Fluorescent Dyes. *Chem. – Eur. J.* **2005**, *11*, 3959–3967.

(8) Alessi, A.; Salvalaggio, M.; Ruzzon, G. Rhodamine 800 as Reference Substance for Fluorescence Quantum Yield Measurements in Deep Red Emission Range. *J. Lumin.* **2013**, *134*, 385–389.